Sensors and Materials, Vol. 38, No. 3 (2026) 1153–1179
MYU Tokyo

S & M 4369

Distributed Optical Fiber Strain Field Reconstruction Method for Prefabricated Beam Bridges Based on a Physics-guided PINN

Yandong Dong,[1] Sheng Zhang,[1] Qiang Li,[1] and Yang Liu[2*]

[1]China Energy Transport Technology Research Institute Co., Ltd., Beijing 100089, China
[2]School of Transportation Science and Engineering, Harbin Institute of Technology, Harin 150090, China

(Received December 4, 2025; accepted February 12, 2026)

Keywords: prefabricated girder bridge, strain-field reconstruction, distributed fiber-optic sensing, physics-informed neural network (PINN)

Sensing the spatial strain field of prefabricated girder bridges remains a major challenge in structural health monitoring because sensors are typically installed on only a subset of individual girders, making it difficult to capture full-bridge field information. To address this issue, in this study, a distributed fiber-optic strain-field reconstruction method for prefabricated girder bridges that is based on a physics-guided physics-informed neural network (PINN) is proposed. The core idea is as follows. First, vehicle-borne monitoring data are used to develop a nonuniform composite Poisson traffic load model, enabling the quantitative characterization of the spatial correlation of strains among multiple girders under realistic traffic flow. This spatial correlation—which represents the lateral load distribution behavior of the bridges—is then embedded into the physics-guided PINN framework as a physics-based constraint. Consequently, the network is guided to extrapolate strain responses from instrumented girders equipped with distributed optical fibers to uninstrumented girders, thereby achieving full-bridge strain-field reconstruction. Both scaled model tests and field monitoring data demonstrated that the proposed method can effectively reconstruct physically consistent spatial strain fields, which can serve as the basis for subsequent structural condition assessment.

1. Introduction

Bridge structural health monitoring (SHM) has received extensive attention because it enables the continuous acquisition of structural responses under operational conditions and provides timely insight into changes in structural performance.[1–3] However, in long-term practical monitoring, economic constraints often limit sensor deployment to only a subset of girders, making it difficult to obtain the global structural response. This limitation significantly undermines the reliability and effectiveness of SHM systems. Consequently, a key challenge in the field is how to accurately reconstruct the full structural response field from incomplete and noise-contaminated local measurements. Solving this problem is essential for achieving the precise condition evaluation and intelligent maintenance of bridge structures.

*Corresponding author: e-mail: ly7628@hit.edu.cn
https://doi.org/10.18494/SAM6097

ISSN 0914-4935
https://myukk.org/

Among the various structural responses, strain—being a direct indicator of the stress state—has drawn significant attention in the development of full-field reconstruction methods. Traditional approaches typically rely on accurate physics-based finite element models. For example, Huang *et al.* proposed a sparse Bayesian learning framework that incorporates probabilistic basis selection and adaptively filters relevant basis functions using sparse priors;[4] however, its performance still heavily depends on the accuracy of the initial finite element model. In practice, uncertainties in parameters, simplified boundary conditions, and potential structural damage introduce modeling errors that inevitably degrade reconstruction accuracy.

To reduce the dependence on highly accurate physical models, data-driven approaches have gained increasing traction. He *et al.* integrated temporal convolutional networks with Gaussian processes to develop a Gaussian process-temporal convolutional network model for predicting the dynamic responses of vehicle–bridge interaction systems under stochastic excitations.[5] Their method effectively captures long-term temporal dependences and leverages Gaussian processes to quantify uncertainties in both the system and the excitation, thereby enhancing prediction robustness in complex environments. Li *et al.* further developed a full-field response reconstruction method based on singular value decomposition and pseudoinverse operators. By extracting dominant modal components from measurement data and combining them with multiscale finite element modeling, their approach enables high-accuracy reconstruction of strain and displacement fields from limited sensing points, significantly improving analysis efficiency for large-scale structures.[6]

In recent years, generative deep learning models have demonstrated strong capabilities in fitting complex data distributions. Shu *et al.* introduced conditional diffusion models into response reconstruction and proposed the DF-CDM method, which leverages forward diffusion and reverse denoising processes combined with fused time–frequency conditional inputs. Compared with generative adversarial networks, this approach significantly improves the dynamic response reconstruction quality under severe sensor sparsity and results in more stable training.[7] Jiang *et al.* explored the long-term strain prediction of concrete structures using meteorological data and convolutional neural networks, and established nonlinear mappings between temperature, humidity, wind speed, and time-dependent strains.[8] Their method effectively predicts shrinkage and creep effects, reducing the need for costly static tests. Wu *et al.* employed generalized regression neural networks to construct surrogate models that replace parameterized finite element analysis and calibrated them using dynamic testing data, accurately predicting static stress responses.[9] Oh *et al.* utilized convolutional neural networks to learn strain–response relationships between structural components and selected optimal models through correlation analysis, enabling reliable strain prediction for adjacent elements.[10]

The construction of stochastic traffic flow models is fundamental for evaluating the dynamic responses and fatigue reliability of long-span bridges during operation. With advancements in SHM technologies, data-driven refined modeling approaches have garnered increasing interest. Traditional traffic simulations typically employ Monte Carlo methods, but they often overlook the intrinsic correlation between vehicle arrival sequences and axle loads, resulting in discrepancies from real traffic flow. Through an analysis of weight-in-motion data, Di *et al.* revealed strong correlations between vehicle-type transition probabilities and the axle loads of

multiaxle vehicles.[11] They proposed a correlation-informed stochastic traffic flow generation method that integrates Markov chain Monte Carlo techniques with correlated random sampling, significantly improving the realism of traffic flow simulations and providing more accurate load inputs for the dynamic response analysis of long-span suspension bridges.

Under traffic load, long-term strain responses are essential indicators for evaluating the service performance of bridges; however, monitoring data often contain missing values because of equipment malfunction or transmission interruption. To address this issue, Chen *et al.* developed a hybrid deep learning–autoregressive model that employs bidirectional gated recurrent units and convolutional neural networks to capture the spatiotemporal correlations of strain data.[12] The model further incorporates strong temperature–strain dependence to reconstruct missing long-term monitoring data. As time goes by, the performance of structural health monitoring systems will be affected by environmental factors and internal degradation, resulting in time-varying behaviors. Bartels and Marx studied the impact of aging on the measurement system and proposed a new method to compensate for these time-related effects.[13] They introduced a compensation method based on Bayesian model updating, effectively addressing the drift in measurement accuracy over time. Its effectiveness was verified using field data from the Huanpu Bridge South Steel Box Girder Suspension Bridge, which demonstrated high reconstruction accuracy and ensured data completeness for traffic-load effect analysis. Liang and Xiong on the basis of the measured traffic data from weigh-in-motion (WIM), established a probability model for key parameters such as total vehicle weight and vehicle spacing, and used the Monte Carlo method to generate dynamic stochastic traffic flow with multiple parameters. Subsequently, they applied DRTF to the calculation of the maximum vehicle load effect in the bridge influence line, which was used to evaluate the load adaptability of existing highway bridges under different traffic volume conditions during the operational period.[14]

In recent years, deep learning has attracted considerable attention in structural response reconstruction because of its powerful feature-extraction and nonlinear-fitting capabilities.[15–17] The physics-informed neural network (PINN), an emerging paradigm that integrates physical laws with data-driven learning, offers new possibilities for SHM. By embedding governing equations, boundary conditions, and initial conditions into the loss function, the PINN enables neural networks to simultaneously satisfy data fidelity and physical constraints during training, thereby achieving high-accuracy predictions and solving inverse problems even with limited or unlabeled data. In the context of moving-load response analysis of bridges, Al-Adly and Kripakaran employed a PINN to solve fourth-order partial differential equations and successfully predicted the dynamic responses of simply supported beams under moving loads while optimizing hyperparameters through sensitivity analysis.[18] Liu *et al.* proposed a PINN architecture composed of a trainable data-driven layer and a nontrainable model-driven layer capable of identifying moving forces directly from structural responses without prior knowledge of load information.[19] Li *et al.* constructed a PINN framework based on Kirchhoff–Love plate theory for baseline-free damage identification in plate structures, where the Teager energy operator was employed to amplify local anomalies and effectively localize damage.[20] Collectively, these studies revealed that the PINN, by incorporating physical priors with

monitoring data, can effectively address forward and inverse problems in SHM, and provide a highly accurate, generalizable, and computationally efficient pathway for structural condition assessment, damage detection, and service-life prediction.

From early physics-based methods that rely on finite element models to recent advancements in deep learning and generative modeling and further, to emerging PINN frameworks that combine physical priors with data-driven learning, researchers have made notable progress in improving prediction accuracy, reducing model dependence, and enhancing generalization. Nevertheless, most existing studies still rely on static or idealized traffic assumptions and fail to capture the stochastic and multiaxle-correlated nature of real traffic loads, resulting in limited adaptability under complex operational conditions. Moreover, constructing physically meaningful constraints tailored to the mechanical characteristics of bridge structures remains a key challenge.

To address these limitations, we propose a physics-guided neural network framework for distributed fiber-optic strain-field reconstruction in prefabricated girder bridges. The key innovation lies in embedding stiffness distribution and intergirder correlation characteristics, derived from transverse load-sharing behavior, as mechanically motivated regularization constraints within the learning framework. First, a composite Poisson traffic flow model is constructed using real monitoring data. Strain responses from instrumented girders equipped with distributed optical fiber sensors (DOFSs) are then used to guide spatial extrapolation to uninstrumented girders. The proposed method is validated through scaled model tests and further, applied to an in-service bridge. The results demonstrate that the method can effectively reconstruct physically consistent full-bridge strain fields, offering a new approach for evaluating the structural state of prefabricated girder bridges.

2. Algorithm Theory

To enable strain-field reconstruction for prefabricated girder bridges, a composite Poisson-based stochastic traffic flow model is first established using site-specific measured vehicle load data. The probability distribution functions and corresponding parameters are derived to accurately represent the statistical characteristics of the traffic stream. On the basis of the vehicle load information collected from the bridge's WIM system—including the vehicle class, gross vehicle weight, and intervehicle spacing—a probabilistic model tailored to the local traffic conditions is constructed.

Moreover, the lateral load-sharing behavior of the prefabricated girder bridge is characterized by explicitly considering the stiffness distribution among individual girders. The strain correlations between adjacent girders are analyzed, and the corresponding Pearson correlation coefficients are computed to quantify their mechanically induced response dependence. Rather than being treated as governing physical laws, these correlation measures are incorporated into the learning framework as physics-guided regularization terms. By jointly accounting for the structural stiffness characteristics, data-misfit terms, and the stochastic vehicle-load distribution model, a comprehensive loss function is constructed to guide network training toward mechanically consistent predictions.

When a vehicle passes over the weighing section, the strain-based sensors embedded in the WIM system generate electrical responses proportional to the load-induced deformation. These weak electrical signals are first amplified and conditioned, and subsequently digitized by the data acquisition unit, resulting in time-history records that reflect the dynamic load effects of individual axles.

The passage of each axle produces a distinct response in the measured signal, from which axle events are identified on the basis of characteristic peaks in the processed signal. Representative signal features associated with each axle, such as peak magnitude or integrated response, are then extracted and related to axle loads through a calibrated transfer relationship. The gross vehicle weight is obtained by summing the estimated axle loads, while the measured vehicle speed is used to ensure consistency in axle spacing and vehicle configuration.

System calibration is performed using reference vehicles with known axle and gross vehicle weights. Calibration parameters are determined by minimizing the discrepancy between the measured electrical responses and the corresponding known loads under representative operating conditions. Both static and dynamic calibrations at different vehicle speeds are considered to account for speed-dependent effects and sensor characteristics. Periodic recalibration and quality-control procedures are applied to mitigate the effects of sensor drift, environmental variations, and long-term aging, thereby ensuring the reliability of the WIM-derived traffic load data used in subsequent stochastic modeling.

2.1 Modeling method for stochastic vehicle loads based on a nonhomogeneous compound Poisson process

2.1.1 Acquisition of vehicle weight-in-motion data

A WIM system is employed to record truck weights. When a truck passes over the weighing platform, the resistance strain sensor generates a weak electrical signal, which is subsequently amplified by a signal-conditioning circuit. The processed weight information is then stored on a data acquisition card. The vehicle parameter dataset used in this study was collected via the WIM system throughout 2021. The recorded parameters include the truck arrival time, vehicle classification, gross vehicle weight, axle load, and travel speed. On the basis of the relationship between the arrival time of a given truck and the speed of the following truck, the intervehicle spacing for each vehicle can be determined. In accordance with the predefined error-handling criteria, any measurement with error exceeding three times the standard deviation was discarded and replaced with the arithmetic mean.

2.1.2 Random traffic flow model

The arrival of vehicular load events on highway bridges is random with respect to time, and each load event occurs independently of the others. When a compound process is employed to characterize the operation of vehicle load, two assumptions must be satisfied: (a) the vehicular loads within the time interval [0, T] follow an identical probability distribution; (b) vehicles

travel along a single lane. Under these assumptions, the mathematical representation of the process can be described using a Poisson distribution.

To more accurately represent real traffic flow on bridges, the Poisson vehicle-load model must be extended to a nonhomogeneous compound Poisson process, where the variable $N_i(t)$ denotes the number of events in the Poisson process. A larger M value corresponds to a more refined stochastic representation, thereby improving the accuracy of the simulated traffic load process.

$$s(t) = \sum_{i=1}^{M} \sum_{n=0}^{N_i(t)} \zeta_{jn} \cdot I\left(t; \tau_{jn}\right) \tag{1}$$

Here, $s(t)$ represents the random traffic load acting on the bridge at time t; M denotes the number of time intervals; $N_i(t)$ represents the i-th nonhomogeneous Poisson process over the interval $[T_{i-1}, T_i]$; $\lambda(t)$ is the rate function of the process; and ζ_{jn} represents the weight of the j-th vehicle belonging to the n-th arrival category. In addition, τ_{jn} denotes the duration for which the j-th vehicle of category n remains on the sensor as it passes over it.

If the time interval between two successive vehicles follows an exponential distribution (2), the Poisson process can be used to characterize the stochastic nature of vehicular loading. The probability density function (PDF) of the interarrival time can be expressed as

$$f_i(T) = \begin{cases} \dfrac{1}{\lambda_i} e^{-(1/\lambda_i)T}, & T \geq 0 \\ 0. & T < 0 \end{cases} \tag{2}$$

Here, λ_i is the parameter of the exponential distribution.

On the basis of the actual traffic flow density data over time provided by the WIM system, the parameters λ_i for different time intervals can be determined, thereby enabling the construction of the Poisson process model.

2.1.3 Probabilistic distribution model of vehicle loads

Vehicle weight is among the most critical parameters of traffic loads and significantly affects the design and assessment of transportation infrastructures such as roads and bridges. There are multiple types of vehicles traversing bridges, and each type may operate under different loading conditions such as fully loaded, empty, or partially loaded states. As a result, vehicle loads exhibit a multimodal distribution.

A Gaussian mixture model (GMM) is a probabilistic model used to describe a combination of multiple Gaussian (normal) distributions.[21] In a GMM, it is assumed that the observed data are generated from several Gaussian components, with each component representing a subgroup or cluster within the data. Previous studies have demonstrated that GMMs can approximate arbitrary probability distribution functions, making them suitable for characterizing the probability distribution of vehicle loads. A GMM can be expressed as

$$G(\boldsymbol{u} \mid \boldsymbol{\mu}) = \sum_{k=1}^{P} w_k \frac{1}{\sqrt{2\pi}\sigma_k} \exp\left[-\frac{\left(u - \mu_k\right)^2}{2\sigma_k^2} \right]. \tag{3}$$

Here, w_k denotes the weight of the k-th Gaussian component, μ_k and σ_k represent the mean and standard deviation of the k-th Gaussian distribution, respectively, and P is the total number of Gaussian components.

The wheelbase of vehicles follows a lognormal distribution. Similarly, the lognormal distribution can also describe the PDF of the vehicle speed. In a GMM, increasing the number of components allows for the model to better approximate the true distribution; however, it also increases model complexity. To determine an appropriate number of Gaussian components, the Bayesian information criterion (BIC) is employed. The P value corresponding to the minimum BIC is selected as the optimal number of Gaussian components. The BIC is calculated as

$$V_{BIC} = r \ln s - \ln L\left(q \mid M, A_i, \mu, \sigma^2\right). \tag{4}$$

Here, r denotes the number of parameters in the mixture model, s represents the length of the observation sample vector, and L corresponds to the maximum likelihood value.

On the basis of the WIM system data, a nonhomogeneous compound Poisson process model was established to represent stochastic traffic flow. Moreover, the parameters of the GMM for the measured vehicle weights were determined using Eq. (3), thereby constructing a stochastic vehicle-load model under realistic traffic conditions.

2.2 Construction of physical constraints on transverse strain correlation characteristics of main girders

In this section, a PINN is constructed to characterize the mechanical correlation between adjacent primary girders under vehicle loading. The proposed network incorporates the transverse stiffness ratios between the girders and the Pearson correlation coefficients between the edge and middle girders as key physical constraints, and embeds them directly into the loss function to introduce structural mechanics knowledge during training. This approach effectively enhances the prediction accuracy and generalization capability of the model while also improving the physical interpretability of the network, ensuring that the predicted strain responses are consistent with the actual load-transfer behavior of multigirder bridges.

2.2.1 Transverse distribution factors and intergirder coordination

When vehicles traverse a bridge composed of multiple T-shaped girders, the loads are transmitted both longitudinally and transversely, and all T-girders participate to varying degrees in carrying the vehicle weight. Under a load P applied on the bridge, the transverse stiffness of the structure inevitably induces load transfer along both the x- direction and y-directions,

meaning that all the primary girders contribute to the load distribution to different extents. Considering the spatial complexity of the girder system, it is reasonable to transform the complex three-dimensional problem into an equivalent planar problem as follows.

$$S = P \cdot \varphi(x, y) \approx P \cdot \varphi_1(x) \cdot \varphi_2(y) \tag{5}$$

Here, S represents the effect of the applied load, $P \cdot \varphi(x, y) \approx P \cdot \varphi_1(x) \cdot \varphi_2(y)$ denotes the influence surface of the bridge internal forces, and $\varphi_1(x)$ and $\varphi_2(x)$ correspond to the internal force influence line functions of the individual girders.

For practical engineering applications, obtaining the stiffness of individual girders in an actual bridge is straightforward. Let P_v denote the force or equivalent internal force of the v-th transverse girder. According to the stiffness distribution theory in statics, it can be expressed as

$$D_v = \frac{K_v}{\sum_{k=1}^{w} K_k}. \tag{6}$$

Here, D_v denotes the distribution factor of the v-th girder, K_v the stiffness of the v-th girder, and K_k the stiffness of the k-th girder.

2.2.2 Strain correlation analysis based on the Pearson coefficient

In prefabricated girder bridges, a certain relationship exists among the mechanical responses of multiple girders. To characterize this relationship, the correlation between a target structural component and its adjacent components was investigated. By establishing such correlations, the strain response of a specific target girder can be estimated using the responses of multiple neighboring girders. Given the large number of girders in a bridge, a considerable number of measurement points can be associated with the target component and utilized for monitoring. Under specific dynamic loads, the structural response correlation between the target girder and its neighbors becomes highly complex because of factors such as location, dimensions, structural behavior, and applied loads. It is therefore necessary to identify the associations between the target girder and the measured points of known girders to accurately predict the structural response and evaluate the safety of the target component.

Prior to constructing the PINN, the correlation between the strain responses of the target girder and the known primary girders is analyzed. The neural network is then configured to map the strain responses of the known girders to the target girder, forming an optimal PINN for estimating the strain response of the target girder.

Assume that there are c measurement points on a given edge girder. At d discrete time instances, the strain values of these measurement points collectively form the following matrix $\boldsymbol{A}$:

$$\boldsymbol{A}=\begin{bmatrix} \varepsilon_{11} & \varepsilon_{12} & \cdots & \varepsilon_{14} \\ \varepsilon_{21} & \varepsilon_{22} & \cdots & \varepsilon_{24} \\ \cdots & \cdots & \cdots & \cdots \\ \varepsilon_{c1} & \varepsilon_{c2} & \cdots & \varepsilon_{cd} \end{bmatrix}. \tag{7}$$

Here, ε_{cd} represents the strain at measurement point c at time instant d.

The observation vector at time t satisfies the following condition:

$$\boldsymbol{x}_t=\left[\varepsilon_{t1},\varepsilon_{t2},...,\varepsilon_{tc}\right]. \tag{8}$$

Let e denote the number of measurement points on the girder to be predicted. The strain values of these points over g time instances are collectively represented by matrix $\boldsymbol{B}$.

$$\boldsymbol{B}=\begin{bmatrix} \varepsilon_{11} & \varepsilon_{12} & \cdots & \varepsilon_{14} \\ \varepsilon_{21} & \varepsilon_{22} & \cdots & \varepsilon_{24} \\ \cdots & \cdots & \cdots & \cdots \\ \varepsilon_{e1} & \varepsilon_{e2} & \cdots & \varepsilon_{eg} \end{bmatrix} \tag{9}$$

Let the linear combination coefficients be represented by the vector $\boldsymbol{w}\in\mathbb{R}^m$. The predicted values can then be expressed as

$$\hat{\boldsymbol{y}}=\boldsymbol{w}^{\top}\boldsymbol{x}. \tag{10}$$

where $\hat{\boldsymbol{y}}$ represents the predicted value at a specific location point.

$$\bar{\boldsymbol{x}}=\frac{1}{N}\sum_{t=1}^{N}\boldsymbol{x}_t \tag{11}$$

Here, $\bar{\boldsymbol{x}}$ represents the mean strain of the known measurement points.

The predicted mean at each time instant is expressed as

$$\bar{z}_k=\frac{1}{N}\sum_{t=1}^{N}z_{tk}\ . \tag{12}$$

After centering the target vector, we obtain

$$\widetilde{\boldsymbol{X}}=\boldsymbol{X}-\mathbf{1}_N\bar{\boldsymbol{x}}^{\top}. \tag{13}$$

Here, $\widetilde{\boldsymbol{X}}$ represents the matrix $\boldsymbol{X}$ after mean centering, $\mathbf{1}_N$ denotes an N-dimensional vector of ones, and K represents the transpose of a matrix.

By computing the covariance matrix of the input samples, we obtain

$$\boldsymbol{S}_{xx} = \frac{1}{N}\boldsymbol{X}^{\top}\boldsymbol{X} \in \mathbb{R}^{m\times m}. \tag{14}$$

$\boldsymbol{S}_{xx}$ represents the input covariance matrix, reflecting the "common response characteristics between the monitored beams/points" under the action of vehicle loads.

The cross-covariance vector between the input and target k can be expressed as

$$\boldsymbol{s}_{xz}^{(k)} = \frac{1}{N}\boldsymbol{X}^{\top}\tilde{\boldsymbol{z}}^{(k)} \in \mathbb{R}^{m}. \tag{15}$$

$\boldsymbol{s}_{xz}^{(k)}$ shows the cross-covariance vector of $\boldsymbol{X}$ and the target $\tilde{\boldsymbol{z}}^{(k)}$ represents the sequence obtained by subtracting the mean value from the k-th target quantity.

The covariance of target k can be expressed as

$$s_{zz}^{(k)} = \frac{1}{N}\left(\boldsymbol{z}^{(k)}\right)^{\top}\boldsymbol{z}^{(k)}. \tag{16}$$

Here, Pearson correlation is introduced to fit the correlation between the two sets of data. The Pearson correlation coefficient is a measure of the degree of linear correlation between two variables, and its value ranges from −1 to 1. When two variables are positively correlated, the correlation coefficient is greater than 0. When two variables are negatively correlated, the correlation coefficient is less than 0. The closer the value is to 1 or −1, the greater the degree of correlation. If the correlation coefficient is 0, there is no correlation between these two variables. The strain response of the i-th adjacent component among n adjacent components is as follows. The Pearson correlation coefficient between the two responses is defined as

$$r\left(\hat{\boldsymbol{y}}, \boldsymbol{z}^{(k)}\right) = \frac{s_{xz}}{\sqrt{S_{xx}s_{zz}}}. \tag{17}$$

Here, $r\left(\hat{\boldsymbol{y}}, \boldsymbol{z}^{(k)}\right)$ denotes the Pearson correlation coefficient between the predicted value and the known measurement points.

The Pearson correlation coefficient serves as one of the key physical pieces of information for neural network learning. The structural response relationship between the target component and its neighboring components is captured through a PINN. This term enforces consistency between the predicted intergirder strain correlation and the correlation observed in measured data, reflecting transverse load-sharing behavior. A schematic of the algorithm is shown in Fig. 1.

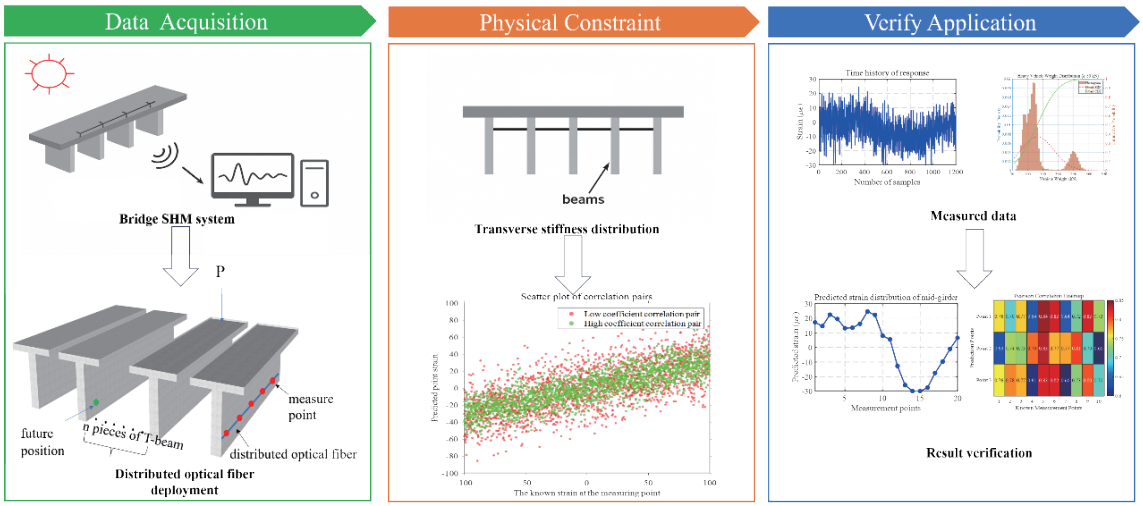

Fig. 1. (Color online) Schematic of the algorithm.

2.3 Single-girder strain extrapolation model based on a PINN

2.3.1 Construction of the loss function

After the transverse strain distribution pattern is obtained, the correlation between the measurement points of the unknown girder and the edge girders is established and incorporated into the loss function as a physics-consistency term. In addition, the structural stiffness characteristics and data prediction error are considered to prevent the model from generating nonphysical predictions that may arise from purely data-driven approaches. Furthermore, by leveraging the probabilistic distribution of vehicle loads, the physical information constraints are modeled stochastically, enabling the network to maintain stable and physically reasonable predictions under diverse loading scenarios.

The mean squared error (MSE) can be expressed as

$$e_{data} = \frac{1}{N}\sum_{i=1}^{N}\left(\hat{\varepsilon}_p^{(i)} - \varepsilon_t^{(i)}\right)^2 . \tag{18}$$

Here, e_{data} represents the prediction error term in the loss function, N is the number of predicted points, $\hat{\varepsilon}_p^{(i)}$ denotes the predicted strain at a point, and $\varepsilon_t^{(i)}$ is the corresponding true strain.

This term ensures the consistency between the network prediction results and the existing measured values. Considering that vehicle loads are a major factor behind the variations in the transverse strain distribution of the bridge, vehicle weight information is further incorporated into the input layer. Here, the Monte Carlo sampling method is employed, with each sample simultaneously sampling a vehicle weight.

An influence matrix $\boldsymbol{H}$ that satisfies

$$\varepsilon = \boldsymbol{H}\boldsymbol{P} + \eta \tag{19}$$

exists. Here, $\boldsymbol{H}$ denotes the influence matrix, $\boldsymbol{P}$ represents the vehicle weight load matrix, and η is the noise term.

Equation (19) provides a simplified linear statistical representation to describe how stochastic vehicle loads affect strain responses, rather than a deterministic forward model. The matrix H represents an equivalent influence operator and is not explicitly identified during training. By establishing a linear mapping relationship between the covariances of vehicle weights and strains, we obtain

$$Cov(\varepsilon) = \boldsymbol{H}Cov(P)\boldsymbol{H}^{\top} + Cov(\eta)\cdot \tag{20}$$

The enhanced physics-based constraint incorporating covariance can be expressed as

$$fcov = \left\| Cov(\hat{\varepsilon}) - \boldsymbol{H}Cov(P_{veh})\boldsymbol{H}^{\top} \right\|_F^2 \cdot \tag{21}$$

Here, *fcov* represents the covariance constraint term between the vehicle weight distribution and the predicted strain results. $Cov(\hat{\varepsilon})$ represents the covariance matrix of the predicted strain. P_{veh} represents a random variable representing the vehicle weight or equivalent vehicle load.

A statistical physical constraint condition was introduced, which guided the strain prediction generated by the network to not only be accurate at individual points, but also to be consistent with the actual structural responses caused by traffic in a statistical sense. The transverse mechanical equilibrium term can be expressed as

$$f_t = \left| \frac{\varepsilon^{\alpha}}{\varepsilon^{\beta}} - \frac{K_{\alpha}}{K_{\beta}} \right|^2 \cdot \tag{22}$$

Here, f_t represents the lateral mechanical equilibrium to the constraint, $\varepsilon^{\alpha}/\varepsilon^{\beta}$ represents the strain ratio at the measurement points of the two single beams with the same cross section, and K_{α}/K_{β} the stiffness ratio between the two single beams.

The data-correlation constraint term can be expressed as

$$f_{corr} = \left| r_{pred} - r_{FE} \right| \cdot \tag{23}$$

Here, r_{pred} denotes the correlation coefficient between the predicted values and the measured data, and r_{FE} represents the correlation inherent in the actual data.

During the optimization of the hidden-layer weights, prior physical knowledge is incorporated. When the prediction deviates from the true value, the model adjusts itself by

increasing the penalty associated with the discrepancy between the predicted data and the physical model within the loss function until the prediction reaches a satisfactory level of accuracy. The loss function of the PINN can be expressed as

$$f_{LOSS} = f_{data} + \lambda_1 f_t + \lambda_2 f_{corr} + \lambda_3 f_{cov} . \tag{24}$$

The loss function of the PINN framework consists of several components: f_{LOSS} represents the overall network loss and is a measure of the deviation between the predicted and actual strain responses; f_{data} denotes the mean squared error between the predicted and measured values; f_t represents the lateral mechanical equilibrium constraint; f_{corr} denotes the correlation constraint between the edge beam and the middle beam; and f_{cov} represents the covariance constraint between the vehicle-weight distribution and the predicted strain response. The parameters λ_1, λ_2, and λ_3 serve as weighting factors for these terms. The weight coefficients λ_1 to λ_3 were introduced to balance the data fidelity and various constraints based on physical priors. After normalizing each loss term, these parameters were selected to ensure the stability of convergence and the comparability of the contributions of different constraints. The same set of weights was used in all case studies, and the results indicated that moderate changes in these parameters would not significantly affect the outcome.

2.3.2 Network architecture

In practical structural health monitoring applications, the available training data are often limited and contaminated by measurement noise. Although the noise itself does not inherently cause overfitting, purely data-driven neural networks with high model flexibility may tend to fit noise patterns when insufficient physical constraints or regularization mechanisms are present. This can reduce generalization capability and lead to physically inconsistent predictions. To address this issue, the proposed method reconstructs the strain field of prefabricated beam bridges by developing a PINN, in which the intergirder strain correlation, vehicle weight distribution, and stiffness distribution are each embedded as independent physical-constraint layers. The PINN serves as a universal function approximator capable of incorporating the governing physical principles underlying the dataset directly into the learning process, thus eliminating the need for extensive training data.

In the proposed framework, the strain data measured from the instrumented girder are used as network inputs, whereas the strain responses at the target girder serve as outputs. The girder stiffness, correlation between the strain responses, and actual vehicle weight distribution are incorporated as physical constraints. Together with the data-driven loss term from the neural network, these components jointly form the total loss function. This total loss is then backpropagated during training, ensuring that the predicted strain responses at the edge girder converge toward the physically consistent responses observed at the middle girder.

The overall network model can be summarized as

$$\hat{\boldsymbol{\varepsilon}} = f_\theta\left(\boldsymbol{\varepsilon_b}, r_\beta{}^\alpha, \frac{K_\alpha}{K_\beta}, W_{inf}\right). \tag{25}$$

Here, $\hat{\boldsymbol{\varepsilon}}$ represents the strain vector at the points to be predicted, $\boldsymbol{\varepsilon_b}$ is the strain vector of the edge girder at a given time, $r_\beta{}^\alpha$ denotes the Pearson correlation coefficient between the girders, K_α/K_β indicates the stiffness ratio between the girders, and W_{inf} represents the vehicle weight distribution information. The Pearson correlation coefficients were computed using synchronized strain time histories of adjacent girders over the same time window, covariance matrices were estimated using sample covariance over selected time windows corresponding to vehicle loading events, the stiffness ratio is calculated from the known cross-sectional characteristics and material parameters, combined with the assumption of linear elastic behavior. The network architecture is shown schematically in Fig. 2.

Training and testing samples were constructed from synchronized strain segments corresponding to vehicle loading events. The dataset was split chronologically to avoid information leakage. The PINN was implemented in Python 3.9 using [TensorFlow]. All strain series were synchronized and normalized using z-score normalization. Training samples were constructed from strain segments associated with vehicle-loading events. The network architecture consists of four hidden layers with 20 neurons per layer and tanh activation. The model was trained using the Adam optimizer (learning rate: 1×10^{-3}) with full-batch training for 500 epochs. Stiffness ratios were treated as constants obtained from structural properties, while Pearson correlation coefficients and covariance matrices were computed from the training dataset and kept fixed during training. To construct training and testing datasets, the strain measurements were first synchronized across all sensing points and segmented according to

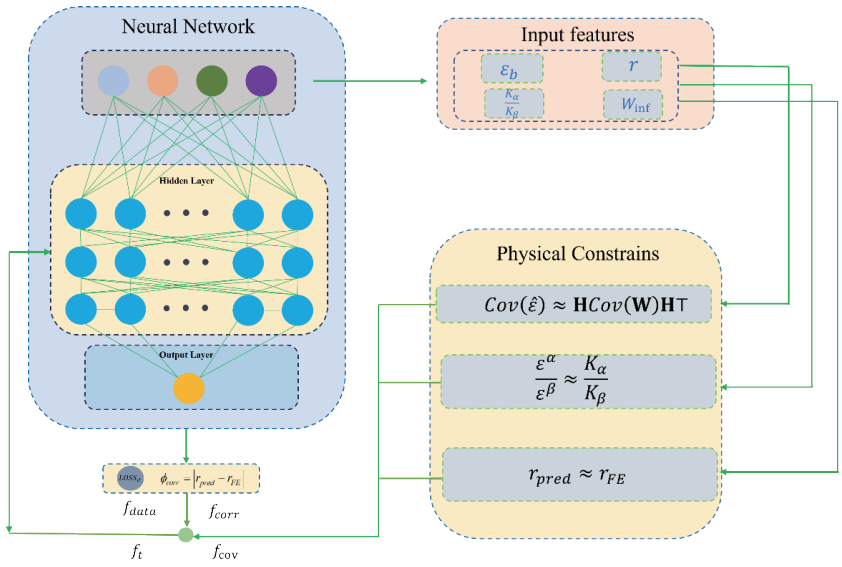

Fig. 2. (Color online) Architecture of the PINN.

vehicle loading events. This network was trained using the Adam algorithm, with a fixed learning rate of $1e^{-3}$. During training, the entire batch training method was adopted. No learning rate scheduler or early stopping mechanism was used, and the model hyperparameters are summarized in Table 1.

In this study, evaluation metrics are introduced to assess the predictive performance of the proposed model. The root mean square error (*RMSE*) and the coefficient of determination (R^2) are employed to evaluate the accuracy of the point predictions.

RMSE measures the deviation between the model predictions and the observed values, while R^2 quantifies the correlation between them. Lower *RMSE* and higher R^2 values indicate more accurate point predictions. They can be expressed as

$$RMSE = \sqrt{\frac{1}{n}\sum_{i=1}^{n}\left(y_i - \mu_{yi}\right)}, \tag{26}$$

$$R^2 = 1 - \sum_{i=1}^{n}\left(\mu_{yi} - y_i\right) / \sum_{i=1}^{n}\left(\mu_{yi} - \overline{y}\right). \tag{27}$$

Here, y_i represents the measured strain, μ_{yi} is the predicted strain, $\overline{y}$ denotes the mean of y_i, and n is the number of samples. The algorithm flowchart is shown in Fig. 3.

Table 1
PINN hyperparameters.

Hyperparameter	PINN model
Hidden layer neurons	(20, 20, 20,20)
Activation function	Tanh
Learning rate	0.001
Max epochs	500
Weight coefficient of loss function (λ_1)	0.1
Weight coefficient of loss function (λ_2)	0.05
Loss function	f_{LOSS}
Relative change amplitude of total loss function ($\mathcal{J}^{(k)}$)	$\mathcal{J}^{(k)} < 10^{-4}$

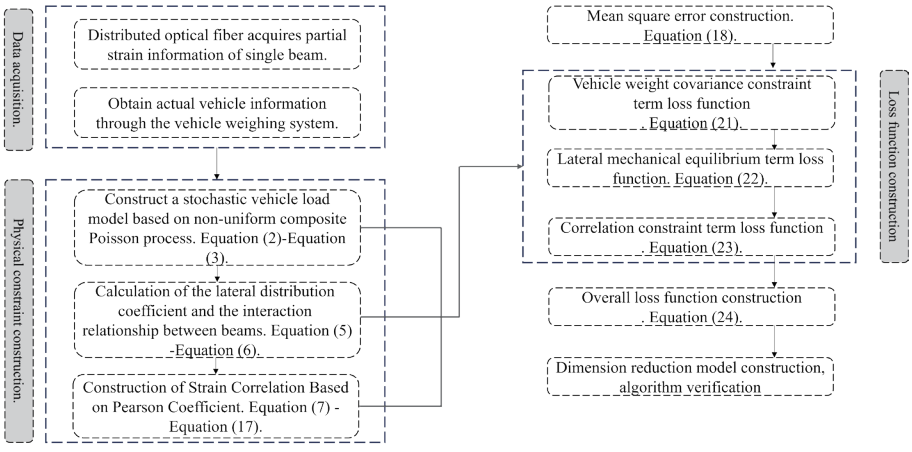

Fig. 3. Flowchart of the proposed algorithm.

3. Case Study Validation

To validate the effectiveness and engineering applicability of the proposed prediction method, a validation study combining a scaled model test and field monitoring data was conducted. First, a three-girder scaled model based on the prototype bridge was constructed. Vehicle loads were applied to simulate the bridge's stress state under actual traffic conditions, and strain time-history data of each girder were acquired using a distributed optical fiber sensors system to serve as training samples for the PINN. A prediction model was subsequently developed on the basis of the obtained experimental data, using the edge girder strain information as input. The strains of the unmonitored girders were then predicted by integrating network learning with physical constraints. Finally, the proposed method was further applied to field monitoring data from an actual bridge to evaluate its practical potential and applicability under real-world conditions.

3.1 Validation using the scaled model

3.1.1 Model design

A scaled model was established on the basis of the principles of similitude theory. The model consists of three prefabricated steel T-girders, whose mechanical properties are listed in Table 2. In the structural testing system, DOFSs were bonded along the longitudinal direction at the bottom of each girder to achieve continuous strain measurements. The fiber optic sensing system operated on the basis of the Brillouin scattering principle with a sampling interval of 20 cm, providing high-spatial-resolution strain distribution data. Strain time-history data under different vehicle load scenarios during the tests were collected to provide the data foundation for subsequent network model training. The test model is shown in Fig. 4.

3.1.2 Vehicle load scenarios

Owing to laboratory testing constraints, a single-vehicle load of 20 kg was used in this study. To simulate the load effects of random traffic as realistically as possible, multiple randomized designs were implemented for the vehicle's travel path, load magnitude, and loading positions during the tests. By varying the lateral position (near the edge or middle girders), longitudinal position, and self-weight configuration of the vehicle, load scenarios with significant differences were generated, reflecting the stochastic distribution characteristics of the vehicle loads.

Table 2
Mechanical parameters of prototype bridge and scaled model.

Item	Prototype bridge	Scaled model	Similarity ratio
Span	35 m	2.5 m	14:1
Flexural stiffness	2.3×10^{16} Pa·mm^4	1.2×10^{12} Pa·mm^4	19166.67:1
Neutral axis height	1425.61 mm	113.51 mm	12.56:1

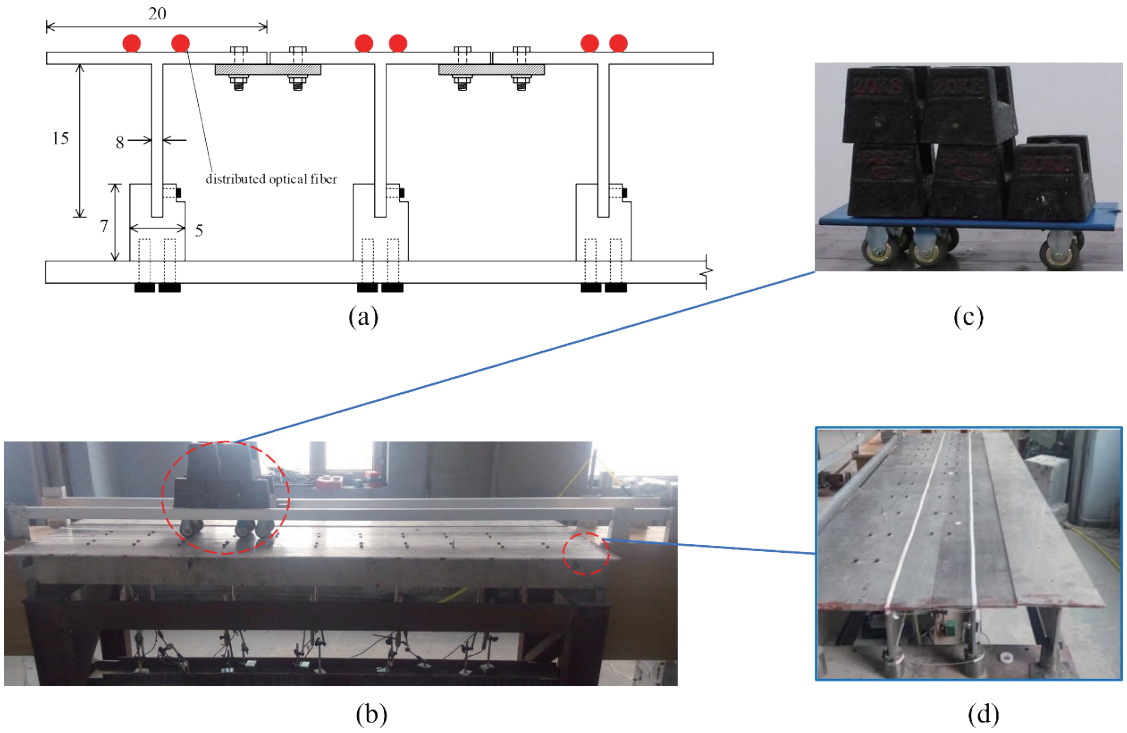

Fig. 4. (Color online) Overall experimental model: (a) schematic of the distributed fiber optic layout, (b) overall experimental model, (c) load trolley, and (d) plan view of the fiber optic layout.

The scaled model is designed on the basis of similitude theory to ensure consistency between the prototype and the model. Geometric similarity is maintained by applying a uniform scaling factor to all structural dimensions and sensor locations. Kinematic similarity is achieved by appropriately scaling time-dependent quantities such as displacement and velocity. Dynamic similarity is ensured by preserving the governing nondimensional parameters related to mass and stiffness, so that the scaled model reproduces the essential dynamic behavior of the prototype.

The loading vehicle was fabricated from alloy steel and scaled in accordance with the prototype vehicle to ensure that the bottom girder strains of the model bridge matched those of the actual bridge. The main parameters of the model vehicle are listed in Table 3.

By varying the lateral position, travel speed, and load of the vehicle, six load scenarios were designed. The strain data of each girder under these scenarios were collected using distributed fiber optic sensors. The load scenario design is summarized in Table 4.

3.1.3 Model prediction results

From the scaled model test data, the strain time history and spatial distribution features of both the edge and middle girders were extracted. Figure 5 shows the time-history curve of the historical strain data of a certain side beam 1. The strain distribution at a position 30 cm above the three girders is shown in Fig. 6. The results indicate that the strain field exhibits notable differences between girders while regular variations in spatial distribution are observed.

Table 3
Parameters of model and prototype vehicles.

Item	Prototype vehicle	Model vehicle	Scale
Weight	15 t	20 kg	125
Wheelbase	1.8 m	128 mm	14
Front-to-middle axle distance	3.8 m	260 mm	14
Middle-to-rear axle distance	1.4 m	100 mm	14

Table 4
Vehicle load scenario settings.

Scenario	Lateral position (distance from left end of model) (m)	Travel speed (cm/s)	Vehicle load (kg)
1	0.05	5	2
2	0.05	5	2
3	0.1	7.5	5
4	0.1	7.5	5
5	0.15	10	10
6	0.15	10	10

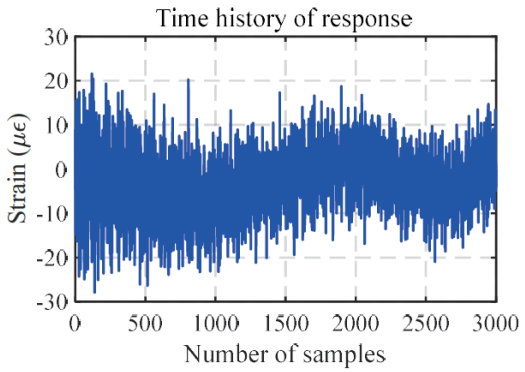

Fig. 5. (Color online) Strain time history of edge girder 1.

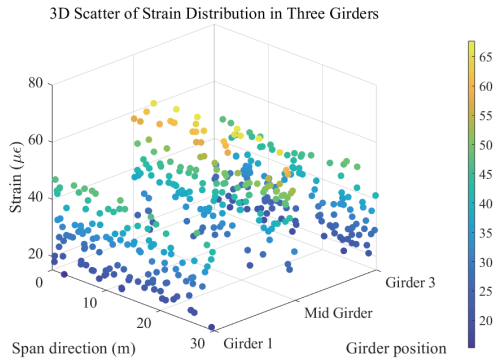

Fig. 6. (Color online) Strain distribution of T-girders.

In this study, strain information from the edge and middle girders at 2000 different time points was selected. To establish the mapping relationship between the middle and edge girders, strain responses from 1800 of these time instances were used as the training set input for the PINN, constraining the model to learn the functional relationship between the two types of girder strains. Considering potential deviations in the scaled model regarding material properties, boundary conditions, and load idealization, all input and output variables were numerically scaled to comparable ranges prior to network training in order to improve optimization stability and convergence by avoiding the effects of differing units and numerical magnitudes. After network training, the remaining two time instances were used as a test set to validate the PINN predictions and assess its ability to estimate responses for unknown samples.

The convergence curve of the loss function during training is shown in Fig. 7(a). The loss decreases rapidly in the early stages. It then stabilizes and continues to decline in the middle and

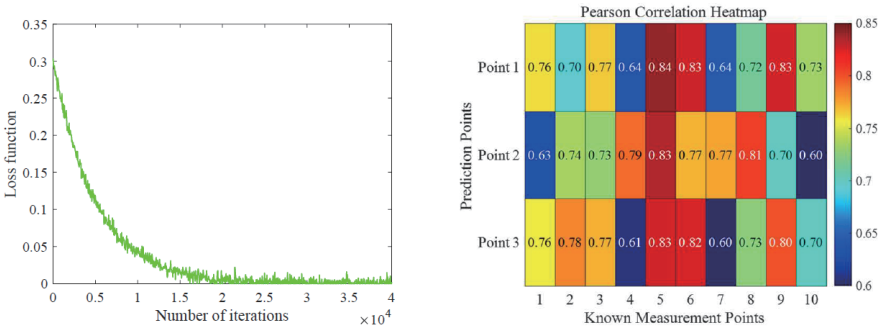

Fig. 7. (Color online) PINN training results: (a) Convergence curve; (b) Pearson correlation heatmap.

later stages, indicating stable convergence behavior and a well-conditioned optimization process. The absence of significant overfitting is further supported by the consistent prediction performance observed on the independent test set. A heatmap of the Pearson correlation coefficients between 10 edge girder measurement points and 3 middle girder measurement points is shown in Fig. 7(b). The heatmap reveals a strong correlation between the edge and middle girders, with correlation coefficients remaining high across different points. This further indicates that the PINN can learn the representative strain relationships between different beams based on the available strain measurements at adjacent monitoring locations. The results show that it has good learning performance on the training set and stable prediction behavior on the test set. On this basis, by utilizing the learned beam-to-beam correlations, the structural responses at unmonitored locations can be inferred. These correlations are based on the measured data from adjacent points.

Strain predictions were performed for the distributed fiber optic measurement points on the middle girder. The prediction results for a representative point are shown in Fig. 8, which shows good agreement between the model predictions and the measured values. After multiple iterations and predictions, a coefficient of determination (R^2) analysis was conducted for the predicted results, as shown in Fig. 9.

3.2 Application to a real bridge

3.2.1 Data sources

The case study is based on a highway bridge with a total length of 556.54 m, whose main structure consists of prestressed concrete continuous box girders. We selected one of the spans of this bridge for monitoring. The structural diagram is shown in Fig. 10. To monitor the bridge's operational state during service, a variety of sensors, including DOFSs, discrete strain gauges, temperature and humidity sensors, displacement sensors, and accelerometers, were installed on the deck and girders, forming a comprehensive multisource monitoring system. In this study, the strain data obtained through the DOFS system's data from the bottom of the webs of the two edge girders were primarily used as inputs, whereas the data from three sets of discrete strain

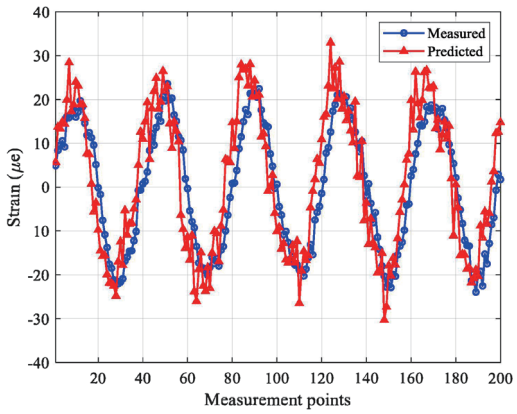

Fig. 8. (Color online) Strain prediction results.

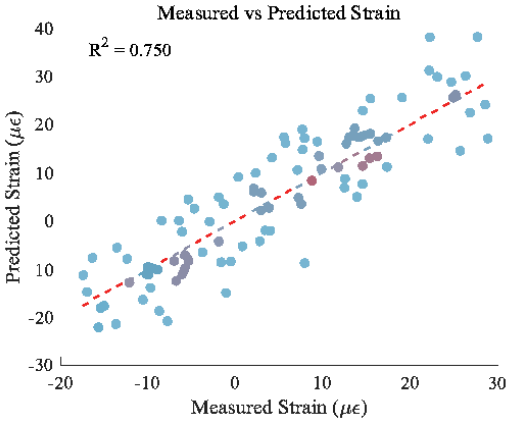

Fig. 9. (Color online) Coefficient of determination of prediction results.

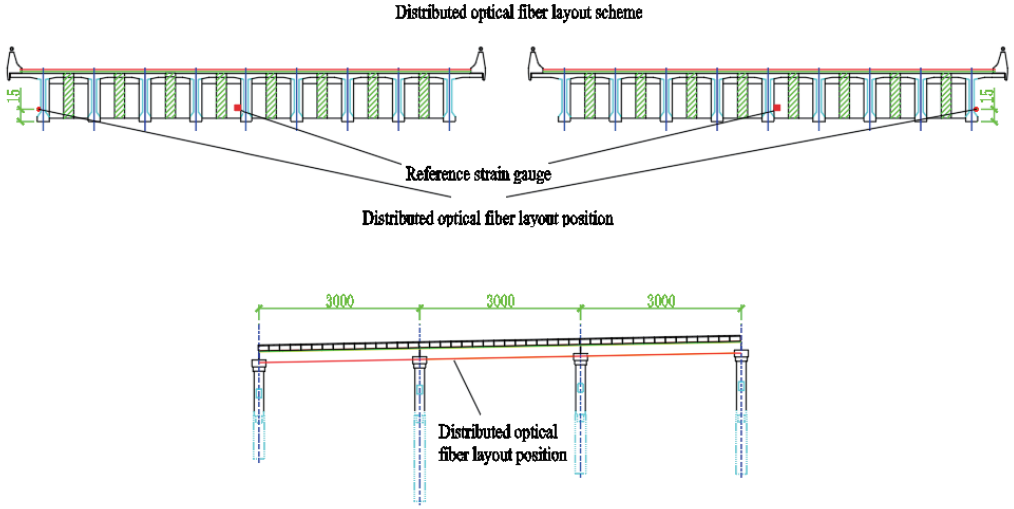

Fig. 10. (Color online) Layout scheme of DOFSs.

sensors on the middle girder were used as references and for validation. This setup enables the establishment of a mapping relationship between edge and middle girder strains and the validation of the effectiveness of the predictive model.

The overall view of the site view is shown in Fig. 11(a), whereas the bridge segment used for monitoring data acquisition is shown in Fig. 11(b). The on-site installation of distributed fiber optics is shown in Fig. 11(c), and a close-up of the fiber installed is provided in Fig. 11(d). The strain data were collected from September to October 2021. During this period, the monitoring data were inevitably affected by multiple factors, including the stochastic effects of vehicle loads, variations in temperature, and measurement noise. In particular, temperature often introduces significant low-frequency effects in strain signals. If unaddressed, these effects can

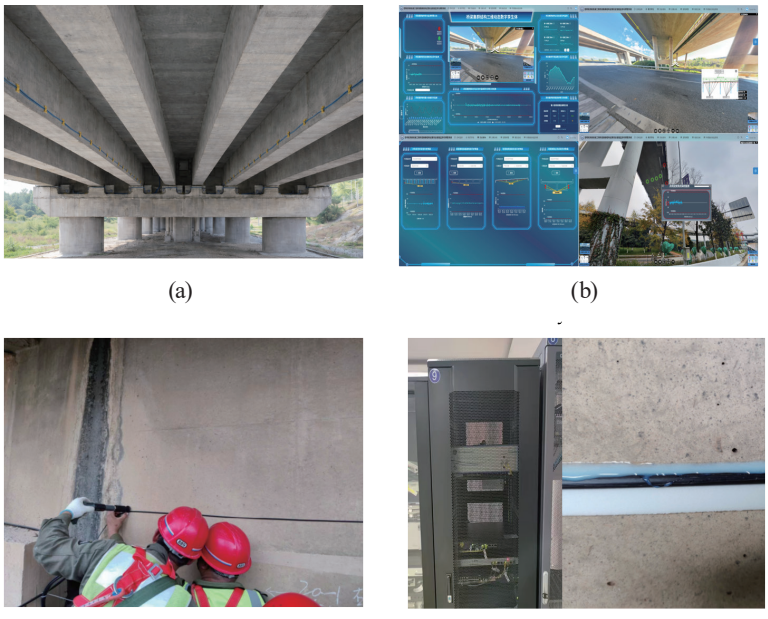

(a) (b)

(c) (d)

Fig. 11. (Color online) Real bridge case: (a) Cross section of the monitored structure, (b) segment of distributed fiber optic installation, (c) on-site installation of distributed fibers, and (d) close-up of installed distributed fiber.

couple structural responses with environmental effects, thereby reducing the accuracy of model training and prediction.

The raw DFOS strain is decomposed into a temperature-dependent component modeled explicitly by a low-order regression on the measured temperature and a traffic-induced residual. To prevent traffic peaks from biasing the regression, the samples detected as events are excluded from model fitting. The denoised strain is obtained by subtracting the fitted thermal component followed by a light outlier suppression filter.

The temperature-induced strain component is fit using a low-order polynomial model:

$$\varepsilon_T(t) = \beta_0 + \beta_1 T(t) + \beta_2 T^2(t). \tag{28}$$

Here, β_0, β_1, and β_2 represent the parameters to be estimated in the regression model. $\varepsilon_T(t)$ represents the strain component caused by temperature. $T(t)$ represents the temperature sensor data sampled simultaneously with the strain. $T^2(t)$ is used to describe the possible nonlinear relationship between temperature and strain.

$$\varepsilon_c(t) = \varepsilon(t) - \varepsilon_T(t) \tag{29}$$

Here, $\varepsilon_c(t)$ represents the strain after temperature compensation.

$$\varepsilon_{den}(t) = Filter(\varepsilon_c(t)) \tag{30}$$

Here, $\varepsilon_{den}(t)$ represents the final denoised strain signal and *Filter*(·) the median filtering operation.

The strain time-history and wavelet-transformed signals for selected measurement points on the two edge girders are shown in Figs. 12 to 15. The analysis of the decomposed frequency components revealed that the temperature-dominated effects are primarily concentrated in the lowest frequency band. By filtering out the low-frequency component during preprocessing, temperature-induced strain interference was effectively removed, allowing for the structural response features related to vehicle loads to be accurately extracted. The application of this method ensures the accuracy and representativeness of the data used for subsequent model training, providing a solid foundation for establishing a reliable strain prediction model.

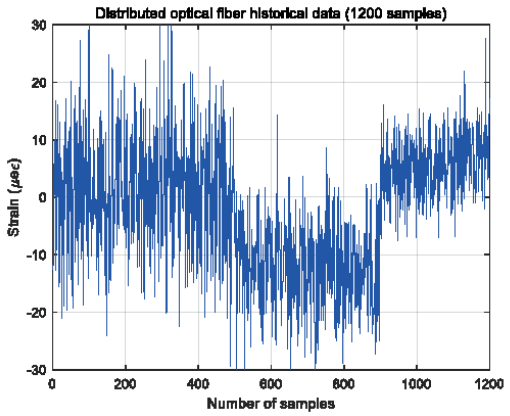

Fig. 12. (Color online) Strain time history of edge girder 1, measurement point 1.

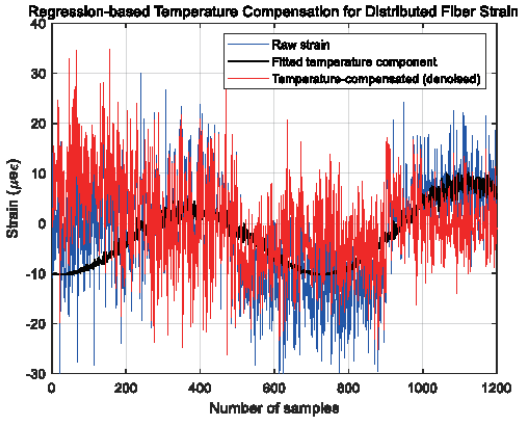

Fig. 13. (Color online) Strain time history of edge girder 2, measurement point 1.

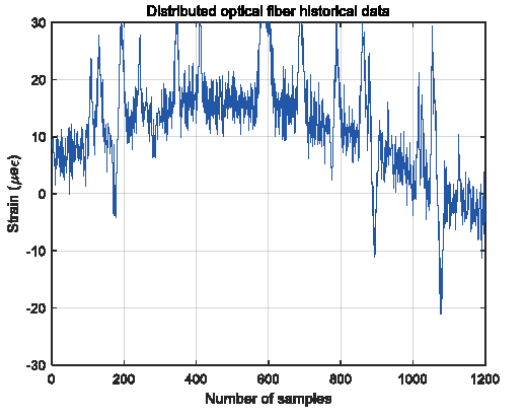

Fig. 14. (Color online) Wavelet-transformed strain time history of edge girder 1, measurement point 1.

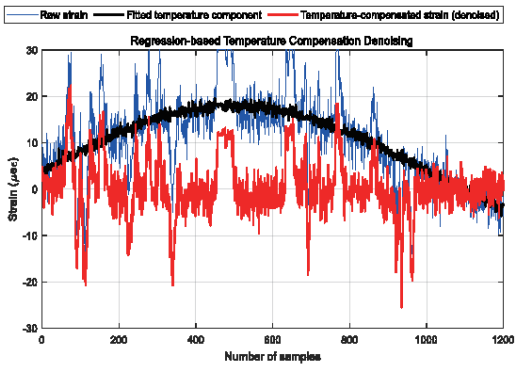

Fig. 15. (Color online) Wavelet-transformed strain time history of edge girder 2, measurement point 1.

3.2.2 Random traffic flow model considering actual vehicle operating conditions

To investigate the characteristics of vehicle loads, we employed a GMM to statistically model the measured vehicle weight data. The PDF and cumulative distribution function (CDF) of the weights of the two-axle trucks are shown in Fig. 16. By comparing the fitting performance characteristics of models with different numbers of components and evaluating them using the BIC, the optimal number of components, *M,* was determined, as shown in Fig. 17. The results indicate that the GMM effectively captures the multimodal characteristics of the vehicle weight distribution, particularly showing a clear concentration in the 75–125 kN range, which represents the primary weight range for two-axle trucks. Compared with a unimodal distribution assumption, the multimodal feature of the GMM better reflects the complexity of actual traffic flows, including variations in vehicle types, loading conditions, and traffic scenarios.

Furthermore, to better characterize the composition of traffic loads, Fig. 18 presents the distribution of measured vehicle types. Vehicle classes A and B mainly correspond to two-axle small vehicles; classes C and D correspond to small passenger cars; and classes E, F, and G represent three-axle or larger heavy trucks. Overall, small vehicles account for the majority of the number; however, in terms of the load magnitude, heavy trucks have a more significant

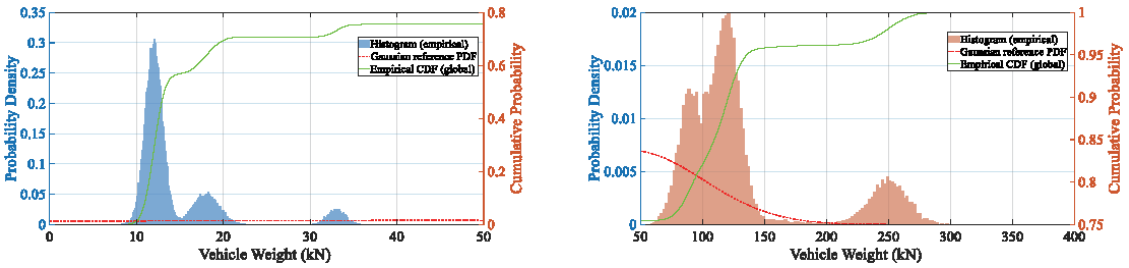

Fig. 16. (Color online) Probability distribution of vehicle weights.

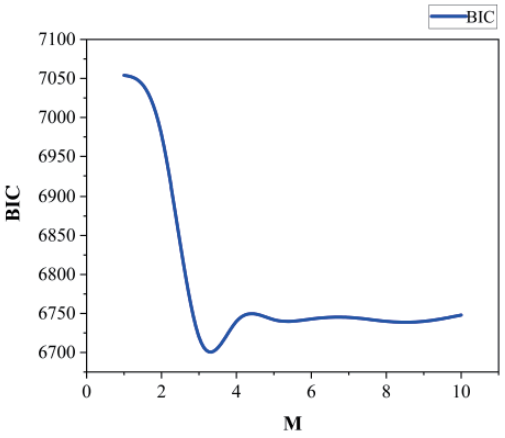

Fig. 17. (Color online) BIC-based determination of the optimal number of Gaussian components.

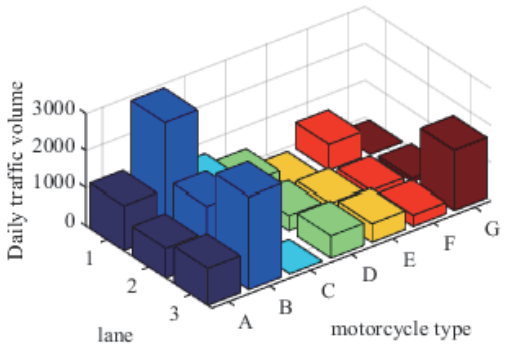

Fig. 18. (Color online) Distribution of different vehicle types.

effect on the bridge structure. By combining the GMM-based vehicle weight distribution with the vehicle type classification, the statistical characteristics of traffic loads can be comprehensively captured, providing essential data support for subsequent structural response analysis and reliability assessment.

3.2.3 Model prediction results

To further validate the applicability and generalization capability of the proposed method in real-world engineering, it was applied to predict strains in an actual bridge structure. First, strain time-history data were obtained from the DOFS system installed at the bottom of the bridge edge beams (beams 1 and 2), which captured the true structural responses under stochastic traffic loads. Owing to the significant transverse coupling between the edge and middle girders, strain variations in the edge girders not only reflect local load effects but also indirectly represent the overall load state of the bridge deck.

On the basis of the previously established prediction model, the measured edge girder strain data were used as input features. Combined with the trained network parameters and correlation matrix information, as shown in Figs. 21(a) and 21(b), predictions were made for the distributed fiber measurements of beams 1 and 9 at two time instances. The strain response at a measurement point on middle beam 5 at a given time is shown in Fig. 21(c), while the strain responses at measurement points on sub-edge beams 2 and 8 at the same time instance are presented in Figs. 21(e) and 21(f), respectively.

To quantitatively validate the accuracy of the proposed strain reconstruction approach, a comparative analysis was conducted between the DOFS measurements and the co-located strain gauge recordings on the middle beam. The strain gauge data were treated as the reference ground truth, while the DOFS-based prediction was obtained under the same loading conditions. The agreement between the measured and predicted strain responses was evaluated using standard error metrics, including the root *RMSE*. As shown in Figs. 19 and 20, the results

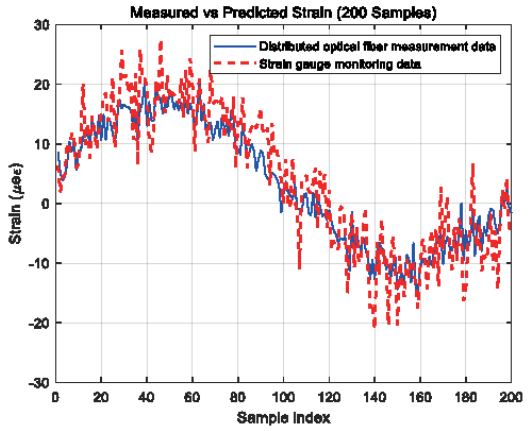

Fig. 19. (Color online) Quantitative comparison of distributed optical fibers and strain gauges.

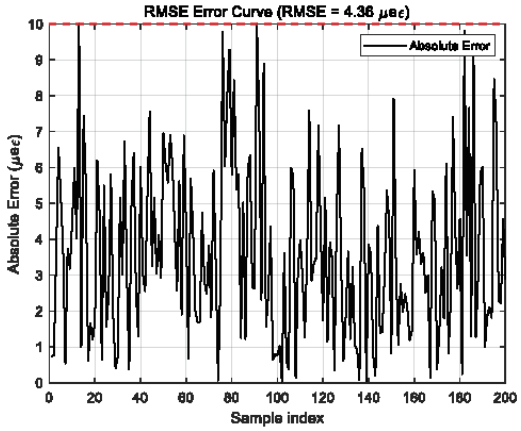

Fig. 20. Quantitative comparison error graph.

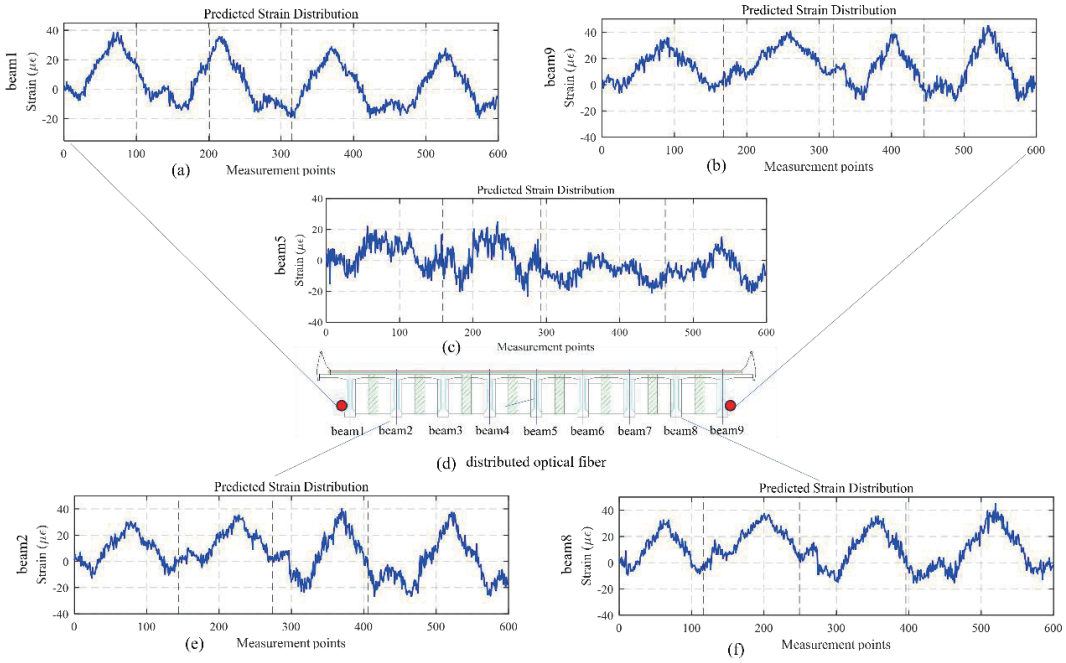

Fig. 21. (Color online) Strain field reconstruction results for an actual bridge.

indicate that the reconstructed strain closely follows the strain gauge measurements, achieving an *RMSE* of approximately 4.35 με, which is within the typical noise level of field DOFS monitoring systems. This quantitative comparison demonstrates the effectiveness and reliability of the proposed method in predicting strain responses for girders with limited or unavailable instrumentation.

The model fully accounts for the transverse load transfer characteristics of the bridge and the correlation patterns between the edge and middle beams, enabling the effective reconstruction of the middle beam strain field even when only partial measurement data are available. The prediction results indicate that the predicted strain variations of the middle beam closely match the actual monitoring data, with high consistency in both peak locations and amplitude distributions, demonstrating the reliability and stability of the method under complex loading conditions.

The application of this prediction approach confirms that, in practical engineering scenarios, the strain states at uninstrumented locations (e.g., middle beam) can be effectively inferred using the data measured from a limited number of edge girder fiber sensors.

Note that the intergirder correlation constraint adopted in this study is based on a linear statistical measure. While this assumption is valid for capturing the dominant transverse load-sharing behavior under typical traffic conditions, it is acknowledged that the actual correlation between girder responses may exhibit nonlinear characteristics under certain scenarios, such as highly variable traffic load, dynamic vehicle–bridge interaction, or modal vibrations of the bridge structure. In such cases, the instantaneous correlation may be reduced, become nonlinear, or even change sign temporarily.

In the proposed framework, the correlation constraint is incorporated as a soft regularization term and is evaluated over time windows rather than at individual time instants. This formulation

Table 5
Quantitative comparison of reconstruction performance.

Scenario	Method	*RMSE* ($\mu\varepsilon$)	R^2
1	Transverse Linear Interpolation	13.86	0.78
2	Regression-based Compensation Method	12.66	0.82
3	Pure Data-driven Neural Network (DNN)	7.25	0.85
4	Proposed Physics-constrained Method	4.35	0.88

prevents transient nonlinear effects or sign changes from dominating the reconstruction process. Moreover, the correlation-based constraint does not act in isolation but complements the physics-informed equilibrium and data-driven terms, thereby enhancing robustness without enforcing strict linear dependence. Consequently, the proposed method remains stable under realistic traffic and dynamic conditions, while its applicability to strongly nonlinear correlation scenarios represents an important direction for future research.

To quantitatively assess the advantage of the proposed physics-constrained reconstruction framework, its performance is further compared with those of several representative baseline methods, including the classical transverse linear interpolation, the regression-based reconstruction approach, and a purely data-driven neural network model without physical constraints. These methods serve as conventional references commonly adopted in strain field reconstruction tasks. The reconstruction accuracy is evaluated using standard quantitative metrics, namely, the root *RMSE* and the coefficient of determination R^2. The comparative results are summarized in Table 5, where it can be observed that the proposed method consistently achieves the lowest reconstruction error and the highest agreement with the measured strain responses, demonstrating the added value of incorporating physics-related constraints.

4 Conclusions

(1) We proposed a bridge strain prediction method based on a PINN. This method is based on random traffic loads and takes into account the correlation between the bridge's lateral strain and the distribution of vehicle weights. A prediction model with physical constraints is constructed, enabling the reconstruction of the strain field at the beam positions of an unmonitored bridge.
(2) The proposed approach can extend strain predictions to an unmonitored single beam, effectively capturing the strain distribution. In scaled model experiments, *RMSE* was 0.8785 and R^2 was 0.75, indicating the high prediction accuracy of the method. In the actual working conditions of bridge structures, the proposed algorithm should demonstrate superior reconfiguration performance compared with traditional methods.
(3) When distributed fiber optic sensing is leveraged, the method is applicable primarily to bridges equipped with comprehensive SHM systems. Increasing the number of measurement points could further improve the accuracy of strain field reconstruction.
(4) In the current study, we relied on a limited set of measured data for training. In future work, we will consider the effects of nonlinear loads, multivehicle interactions, and additional time-varying factors to enhance the model's applicability and robustness under more complex operational conditions.

Acknowledgments

This project is funded by National Energy Shuohuang Railway Research Institute (Grant No: 45 [2024]).

References

1 Y. Liu and M. Gao: Computer-Aided Civil and Infrastruct. Eng. **37** (2022) 1891. https://doi.org/10.1111/mice.12874
2 Q. Xu, X. Ma, and Y. Liu: Computer-Aided Civil and Infrastruct. Eng. **40** (2025) 2695. https://doi.org/10.1111/mice.13459
3 X. Yan, K. Wang, M. Gao, C. Li, and Y. Liu: J. Civil Struct. Health Monit. (2025). https://doi.org/10.1007/s13349-025-00909-x
4 Y. Huang, C. Shao, S. Wu, and H. Li: Smart Mater. Struct. **28** (2019). https://doi.org/10.1088/1361-665X/aae9b4
5 X. He, Y. Zhao, K. Shi, and C. Cai: Eng. Struct. **328** (2025). https://doi.org/10.1016/j.engstruct.2025.119745
6 Y. Li, H. Huang, W. Zhang, and L. Sun: Eng. Struct. **249** (2021). https://doi.org/10.1016/j.engstruct.2021.112986
7 J. Shu, H. Yu, G. Liu, Y. Duan, H. Hu, and H. Zhang: Mech. Syst. Signal Process. **222** (2025). https://doi.org/10.1016/j.ymssp.2024.111783
8 H. Jiang, C. Wan, K. Yang, Y. Ding, and S. Xue: Struct. Health Monit. **21** (2021) 1093. https://doi.org/10.1177/14759217211021942
9 Y. Wu, L. Zhang, H. Liu, and P. Lu: Structures **40** (2022) 812. https://doi.org/10.1016/j.istruc.2022.04.068
10 B. K. Oh, S. H. Yoo, and H. S. Park: Integr. Comput.-Aided Eng. **30** (2023) 395. https://doi.org/10.3233/ica-230714
11 W. Di, Z. Yue, W. Junfeng, W. Qi, and L. Xiaodong: Structures **55** (2023) 1992. https://doi.org/10.1016/j.istruc.2023.07.012
12 C. Chen, L. Tang, Y. Lu, Y. Wang, Z. Liu, Y. Liu, L. Zhou, Z. Jiang, and B. Yang: Eng. Struct. **285** (2023). https://doi.org/10.1016/j.engstruct.2023.116063
13 J.-H. Bartels and S. Marx: Sens. Mater. **37** (2025). https://doi.org/10.18494/sam5393
14 Y. Liang and F. Xiong: KSCE J. Civil Eng. **23** (2019) 3581. https://doi.org/10.1007/s12205-019-2121-8
15 Y.-F. Li, W.-Y. He, W.-X. Ren, and Y.-H. Shao: Adv. Eng. Inf. **65** (2025). https://doi.org/10.1016/j.aei.2025.103215
16 T. Wu, W. Zhu, L. Tang, L. Lang, J. Xu, Q. Yuan, and Z. Zhou: Mech. Syst. Signal Process. **235** (2025). https://doi.org/10.1016/j.ymssp.2025.112961
17 Y. Wang, D. Yang, Y. Yuan, J. Zhang, and F. T. K. Au: Comput.-Aided Civil Infrastruct. Eng. **40** (2025) 3503. https://doi.org/10.1111/mice.13436
18 A. I. F. Al-Adly and P. Kripakaran: Eng. Struct. **338** (2025). https://doi.org/10.1016/j.engstruct.2025.120535
19 J. Liu, Y. Li, L. Sun, Y. Wang, and L. Luo: Eng. Struct. **329** (2025). https://doi.org/10.1016/j.engstruct.2025.119801
20 Z. Li, J. Zhou, H. Nassif, D. Coit, and J. Bae: Reliab. Eng. Syst. Saf. **232** (2023). https://doi.org/10.1016/j.ress.2022.109078
21 S. Li, J. Xin, Y. Jiang, C. Yang, X. Wang, and B. Ran: Adv. Bridge Eng. **5** (2024). https://doi.org/10.1186/s43251-024-00119-3